Single-crystal epitaxial europium iron garnet films with strain-induced perpendicular magnetic anisotropy: Structural, strain, magnetic, and spin transport properties

M. X. Guo,[1,*] C. K. Cheng,[2,*] Y. C. Liu,[1,*] C. N. Wu,[3] W. N. Chen,[1] T. Y Chen,[4] C. T. Wu,[5] C. H. Hsu,[6] S. Q. Zhou,[7] C. F. Chang,[3] L. H. Tjeng,[3] S. F. Lee,[8] C. F. Pai,[4] M. Hong,[2,†] and J. Kwo[1,‡]

[1]*Department of Physics, National Tsing Hua University, Hsinchu 300044, Taiwan*

[2]*Graduate Institute of Applied Physics and Department of Physics, National Taiwan University, Taipei 106216, Taiwan*

[3]*Max Planck Institute for Chemical Physics of Solids, Nöthnitzer Strasse 40, 01187 Dresden, Germany*

[4]*Department of Materials Science and Engineering, National Taiwan University, Taipei 106216, Taiwan*

[5]*Materials Analysis Division, Taiwan Semiconductor Research Institute, National Applied Research Laboratories, Hsinchu 300091, Taiwan*

[6]*National Synchrotron Radiation Research Center, Hsinchu 30076, Taiwan*

[7]*Institut für Ionenstrahlphysik und Materialforschung, Forschungszentrum Dresden, Rossendorf e.V., Bautzner Landstraße 128, 01328 Dresden, Germany*

[8]*Institute of Physics, Academia Sinica, Taipei 11574, Taiwan*

(Received 20 February 2022; accepted 13 May 2022; published 31 May 2022)

Single-crystal europium iron garnet (EuIG) thin films were epitaxially grown on gadolinium gallium garnet (GGG)(001) substrates using off-axis sputtering and showed strain-induced perpendicular magnetic anisotropy (PMA). By varying the sputtering conditions, we have tuned the europium/iron (Eu/Fe) composition ratios in the films to tailor the film strains. The films exhibited an extremely smooth, particle-free surface with a root-mean-square roughness as low as 0.1 nm, as observed by atomic force microscopy. High-resolution x-ray diffraction analysis and reciprocal space maps showed pseudomorphic film growth, a very smooth film/substrate interface, excellent film crystallinity with a rocking curve of 0.012° (ω scans), and an in-plane compressive strain without relaxation. In addition, spherical aberration-corrected scanning transmission electron microscopy showed an atomically abrupt interface between the EuIG film and GGG. The saturation magnetization (M_s) and coercive field (H_c) were measured using a vibrating sample magnetometer. The square-shaped out-of-plane M-H loops in conjunction with angle-dependent x-ray magnetic dichroism demonstrated the PMA in the films. The spin Hall magnetoresistance on Pt/EuIG samples was measured to obtain the PMA field strength ($H_\perp$), which increases from 4.21 to 18.87 kOe with the increasing Eu/Fe ratio and in-plane compressive strain. We also measured spin transport in the Pt/EuIG bilayer structure and directly obtained the real part of spin mixing conductance to be $3.48 \times 10^{14}\ \Omega^{-1}\ \mathrm{m}^{-2}$. We demonstrated current-induced magnetization switching with a low critical switching current density of $3.5 \times 10^6\ \mathrm{A/cm}^2$, showing excellent potential for low-dissipation spintronic devices.

DOI: 10.1103/PhysRevMaterials.6.054412

I. INTRODUCTION

Rare-earth iron garnets, as magnetic insulators (MIs), have played an essential role in the development of spintronics. Previously, yttrium iron garnet (YIG) was widely utilized in spin-wave-related research for the efficiency of magnetic excitation because of its small magnetization damping [1,2]. In addition to spin dynamics, the insulating property led to the discovery of spin Hall magnetoresistance (SMR) [3], which is based on the spin Hall effect in heavy metals (HMs) with strong spin-orbit coupling and the reflection of spin current at the interface between HMs and MIs. Magnetic thin films with perpendicular magnetic anisotropy (PMA) are generally favored for their scalability and stability in magnetoresistive memory devices. Therefore, a MI with a strong PMA offers a great advantage in expanding its industrial applications. However, single-crystal YIG thin films grown on a gadolinium gallium garnet (GGG) substrate possess in-plane magnetic anisotropy, as caused by their large shape anisotropy [4]. Both theoretical [5,6] and experimental [7,8] studies have shown that a suitable substrate may induce lattice strain to give rise to PMA in YIG; the strength, nonetheless, is still weaker than that of its counterparts of thulium iron garnet (TmIG)/GGG [9] and europium iron garnet (EuIG)/GGG [10].

Strain-induced PMA was reported in thin films of TmIG and terbium iron garnet, most of which were grown by pulsed laser deposition (PLD) [11–16]. Wu *et al.* [9,17] employed off-axis magnetron sputtering to deposit TmIG MI thin films with PMA, and studied their magnetic properties and the spin transport properties of HM/TmIG bilayer structures. Furthermore, the PMA of TmIG has enabled the study of breaking time-reversal symmetry in the topological insulator using interfacial exchange coupling [18,19]. Compared to TmIG films, EuIG films have shown greater strength of the PMA field ($H_\perp$) and a larger coercive field (H_c) [10,20].

*These authors contributed equally to this work.
†mhong@phys.ntu.edu.tw
‡raynien@phys.nthu.edu.tw

In this work, we utilized off-axis magnetron sputtering to deposit single-crystal strained EuIG films epitaxially on GGG(001). These films are single crystal with a very narrow full width at half maximum (FWHM) of 0.012° in the rocking curve scans, compared with 0.011° of the GGG substrate; a very smooth surface (with a roughness of 0.1 nm) free of particles; and an atomically sharp EuIG/GGG interface. We have varied the europium to iron (Eu/Fe) ratio (at.%/at.%) from 0.498 to 0.646 to produce an in-plane (IP) compressive strain of −0.77% to −1.04% to tailor the magnetic properties of the EuIG films. The strain has induced PMA in our films, whose strength, as measured/calculated using SMR, increases with the IP compressive strain and the out-of-plane (OOP) tensile strain. The measurements of our EuIG films using vibrating sample magnetometry (VSM) and x-ray magnetic circular dichroism (XMCD) also confirmed the PMA. We fine-tuned the H_c and $H_\perp$ over a much broader range than the previous work of TmIG and EuIG films, providing our EuIG films with versatile applications. For example, although the SMR-induced anomalous Hall effect (AHE) in Pt/EuIG was reported previously [10,20], current-induced magnetization switching has been lacking. By tuning the H_c to a suitable value, and by maintaining good squareness of the AHE loop, we have demonstrated current-induced magnetization switching in the Pt/EuIG bilayer structure.

II. EXPERIMENTAL

EuIG thin films were deposited on GGG(001) substrates by rf magnetron off-axis sputtering with an ∼0.4-nm/min growth rate. The substrates were cleaned with acetone, isopropanol, and deionized water sequentially in an ultrasonic bath. The substrates were then dried under nitrogen gas flow. Each of the cleaned substrates was adhered to a holder with silver paste for better thermal contact during film deposition. The pressure during the deposition (P_{dep}) was 3 to 8 mTorr with a mixture of Ar and O_2 under a flow rate of 40 and 0.7 standard cm^3/min, respectively. EuIG films were deposited at 450 °C, and then we annealed our film in an O_2 ambient at 450 °C for 10 minutes. The film properties were adjusted by varying the longitudinal target-to-substrate distance (L) and P_{dep}. A schematic of the sputtering setup is provided in Supplemental Material Fig. S1 [21].

Atomic force microscopy (AFM) was used to characterize the surface morphology of the films and to determine the film thickness. X-ray diffraction (XRD) using synchrotron radiation was performed at beamline BL13A and BL17B of the Taiwan Light Source at the National Synchrotron Radiation Research Center (NSRRC), Hsinchu, Taiwan, to study the crystallinity, epitaxy, film thickness, and lattice parameters of the single-crystal EuIG films to determine IP and OOP strains of the films. Spherical aberration-corrected scanning transmission electron microscopy (Cs-STEM) was performed to probe the atomic-scale EuIG/GGG interfacial structures. The Eu/Fe ratio of the EuIG films was determined by Rutherford backscattering spectrometry (RBS) in random-geometry measurements using a 1.7-MeV He^+ beam, performed at Helmholtz-Zentrum Dresden Rossendorf, Germany. The backscattered particles were detected at an angle of 170° with respect to the incoming beam direction.

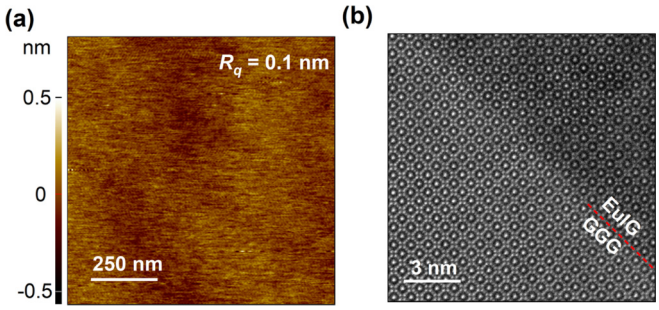

FIG. 1. (a) Surface morphology image of a 24-nm-thick EuIG film grown on GGG(001) showing an R_q of 0.1 nm. R_q stands for RMS roughness. (b) Cs-STEM HAADF cross-sectional image at the interface of EuIG and GGG with zone axis [010]. The red dashed line indicates the interface between EuIG and GGG.

The saturation magnetization (M_s) and the coercive field (H_c) were measured using VSM at room temperature. X-ray absorption spectroscopy (XAS) and XMCD taken at the Fe L_3 edge using a total electron yield mode were conducted at beamline TPS45A of Taiwan Photon Source, NSRRC, Taiwan, to measure the PMA in the EuIG films. The films were magnetized before loading to the end station and were measured with Fe_2O_3 crystals simultaneously in another chamber for the relative energy reference.

SMR transport measurements were carried out in a quantum design physical property measurement system with a rotator capable of angular-dependent magnetoresistance (MR) measurements. Pt/EuIG bilayer samples were fabricated into Hall bars (650 μm × 50 μm) using photolithography, and then were connected to the corresponding channels on the sample holder with copper wire and silver paste.

Current-induced magnetization switching was performed by injecting pulsed currents along the current channel with a pulse width of $t_{\text{pulse}} = 0.05$ s from a Keithley 2400 source meter. Magnetization was monitored by the Hall voltage and collected by a Keithley 2000 multimeter. During the current-induced magnetization switching measurement, an IP magnetic field (H_x) was applied along the current channel to break the domain wall symmetry; and, therefore, the spin torque can drive the domain nucleation and facilitate domain wall propagation [22,23].

III. RESULTS AND DISCUSSION

A. Film morphology, crystal structure, composition, and strain

The study of surface morphology of the EuIG thin films using AFM [Fig. 1(a)] showed a root-mean-square (RMS) roughness as low as 0.1 nm. The atomically flat and particle-free film surface was essential for the subsequent growth of high-quality heterostructures; a recent example is a topological insulator, $(Bi, Sb)_2Te_3$, on EuIG, where an enormous anomalous Hall effect was discovered [24]. A high-angle annular dark field (HAADF) image taken along the [010] direction in Fig. 1(b) shows the epitaxial growth of the EuIG(001) film on the GGG(001) substrate with a nearly perfect EuIG/GGG interface, with no defects and dislocations. The intensity contrast between the EuIG film and the GGG

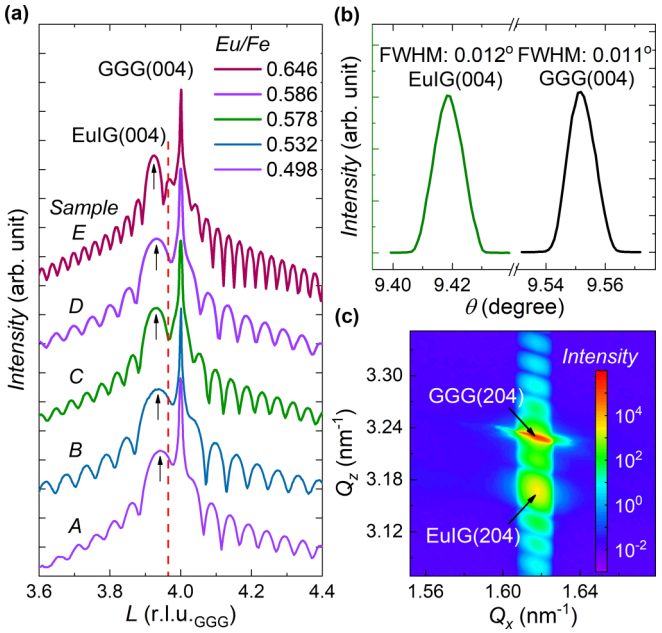

FIG. 2. (a) XRD normal scans for EuIG films grown on GGG(001) substrate with different Eu/Fe ratios, showing clear Laue oscillations. The arrows indicate the position of the EuIG(004) peak. The red dashed line indicates the position of bulk EuIG for reference. (b) FWHMs of rocking curve scans of EuIG(004) and GGG(004) are 0.012° and 0.011°, respectively. (c) RSM for EuIG(204) and GGG(204) diffraction of a 41-nm-thick EuIG film (Sample E).

substrate was caused by the mass difference of the Eu/Fe ratio and the Gd/Ga ratio in EuIG and GGG, respectively.

Figure 2(a) shows the XRD scans along the surface normal (001) for selected EuIG films grown with L varying from 5 cm (Sample A, $P_{\text{dep}} = 3$ mTorr), 6 cm (Sample B, $P_{\text{dep}} = 3$ mTorr), 8 cm (Sample C, $P_{\text{dep}} = 3$ mTorr), and 10 cm (Sample D, $P_{\text{dep}} = 3$ mTorr), and with a higher P_{dep} of 8 mTorr (Sample E, $L = 6$ cm). Note that L is described in Supplemental Material Fig. S1 [21]. The OOP lattice constants ($a_{\perp,f,\text{strained}}$) of Samples A, B, C, D, and E were determined to be 12.561, 12.584, 12.594, 12.600, and 12.624 Å, respectively, with the corresponding film thickness determined from AFM being 33.2, 33.4, 26.4, 25.4, and 41.0 nm, respectively, and from XRD being 29.6, 33.2, 26.9, 26.7, and 41.0 nm, respectively. Note that all the samples are fully strained on the GGG substrate. The reported bulk lattice constant of GGG is 12.382 Å, and that of EuIG is 12.497 Å [25,26]. The red dashed line in Fig. 2(a) shows the peak position of bulk EuIG. The peak positions of the EuIG(004) reflection were at lower angles than that of the GGG(004) reflection in all samples, indicating a larger $a_{\perp,f,\text{strained}}$ of EuIG films than the lattice constant of the GGG substrate and the compressively strained growth of the EuIG films.

Because the relaxed lattice constant is relatively insensitive to the variation of elastic constants for given deformed $a_{\perp,f,\text{strained}}$ and $a_{\|,f,\text{strained}}$, we assumed the same elastic constants in bulk EuIG of different Eu/Fe ratios. The relaxed lattice constants of samples having different Eu/Fe ratios were determined by the equation

$$\frac{c_{11}}{c_{11}+2c_{12}}\frac{a_s - a_{\perp,f,\text{strained}}}{a_{f,\text{relaxed}}} = \frac{a_s - a_{f,\text{relaxed}}}{a_{f,\text{relaxed}}}, \quad (1)$$

where elastic constants c_{11} and c_{12} are 25.10×10^{11} dyne/cm^2 and 10.70×10^{11} dyne/cm^2, respectively; a_s is the lattice constant of the substrate; $a_{f,\text{relaxed}}$ is the lattice constant of relaxed film; and $a_{\perp,f,\text{strained}}$ is the OOP lattice constant of strained film. The relaxed lattice constants of Samples A, B, C, D, and E were calculated to be 12.479, 12.491, 12.496, 12.500, and 12.513 Å, respectively.

The IP strains ($\varepsilon_\|$) and OOP strains ($\varepsilon_\perp$) were calculated by the equations

$$\varepsilon_\| = \frac{a_s - a_{f,\text{relaxed}}}{a_{f,\text{relaxed}}}, \quad (2)$$

where a_s (IP lattice constant of the substrate) is the same as the IP lattice constant of the strained film ($a_{\|,f,\text{strained}}$) because of the fully strained growth of the EuIG films on the GGG substrate, and

$$\varepsilon_\perp = \frac{a_{\perp,f,\text{strained}} - a_{f,\text{relaxed}}}{a_{f,\text{relaxed}}}, \quad (3)$$

respectively. The measured $a_{\perp,f,\text{strained}}$, the calculated relaxed lattice constants, and the IP and OOP strains for Samples A, B, C, D, and E are listed in Table I. As the Eu/Fe ratio in EuIG film increases, the $\varepsilon_\|$ and $\varepsilon_\perp$ increase, respectively.

High crystalline quality in the films is evidenced from the observation of clear and pronounced thickness fringes around the EuIG(004) peak and the narrow FWHM of the rocking curve scans (ω scans) of 0.012°, comparable to that (0.011°) of the GGG substrate in Fig. 2(b).

The sample with the largest $a_{\perp,f,\text{strained}}$ (Sample E) was chosen for reciprocal space map (RSM) measurement. Figure 2(c) shows a RSM around the (204) off-normal reflections of both EuIG and GGG, which is plotted as a function of Q_x and Q_z. The Q_x positions of EuIG(204) and GGG(204) were both located at 1.616 nm^{-1}, indicating that the EuIG film is fully strained on GGG along the IP direction. The epitaxial orientation relationship between the EuIG film and GGG substrate was determined to be EuIG(001)[100]//GGG(001)[100] according to the RSM results from the off-normal diffraction peaks. Moreover, the off-normal phi scan of another sample grown at $L = 6$ cm with the same growth condition as Sample B was taken for verifying the texture of the film to be single crystal. From the Q_z position of the EuIG film and GGG, the $a_{\perp,f,\text{strained}}$ of EuIG was determined to be 12.627 Å, consistent with the value (12.624 Å) determined from the scan along the EuIG(001) direction, as shown in Fig. 2(a). Knowing the different lattice constants of the film and substrate, $a_{\perp,f,\text{strained}}$'s elongation indicates that the film is under an IP compressive strain. Furthermore, the gradual increase in $a_{\perp,f,\text{strained}}$ of the strained epitaxial films indicates that under $P_{\text{dep}} = 3$ mTorr during sputtering, the Eu/Fe ratio in the films varies with the longitudinal target-to-substrate distance in the sputtering chamber, L. We have performed XRD scans on another set of films—Samples A′, B ′, C′, and D′—which were prepared using the same sputtering conditions as Samples A, B, C, and D. The XRD results were similar between the two sets

TABLE I. Structural, strains, and magnetic properties of epitaxial EuIG/GGG(001).

Samples (L; P_{dep})	A (5 cm; 3 mTorr)	B (6 cm; 3 mTorr)	C (8 cm; 3 mTorr)	D (10 cm; 3 mTorr)	E (6 cm; 8 mTorr)	Remarks
Eu/Fe (RBS)	0.498	0.532	0.578	0.586	0.646[a]	
Thickness (nm) (AFM)	33.2	33.4	26.4	25.4	41.0	
Thickness (nm) (XRD)	29.6	33.2	26.9	26.7	41.0	
R_q (nm) (AFM)	0.12	0.15	0.11	0.11	0.30	
$a_{\perp,f,\text{strained}}$ (Å) (XRD)	12.561	12.584	12.594	12.6	12.624 (12.627 from RSM)	[b]
$a_{f,\text{relaxed}}$(Å) (calc.)	12.479	12.491	12.496	12.5	12.513	[c]
$\varepsilon_{\parallel}$(%)	−0.774	−0.873	−0.915	−0.942	−1.044	
$\varepsilon_{\perp}$(%)	0.66	0.745	0.781	0.802	0.89	
M_s (emu/cm^3) (VSM)	72	95	121	125		
H_c(Oe) (VSM)	27	119	158	83		
$H_{\perp}$(kOe) (SMR) (sample; thickness)	4.21 (A″; 9.7 nm)	10.95 (B″; 10.5 nm)	15.97 (C″; 12.5 nm)	18.87 (D″; 13 nm)		[d]

[a]Extrapolated from Fig. 3(a).
[b]A′, B′, C′, and D′ showed similar XRD with A, B, C, D.
[c]Bulk GGG lattice constant, 12.382 Å; bulk EuIG lattice constant 12.497 Å.
[d]B* (12.52 nm) used for XMCD.

of the samples, as shown in Fig. 3(a). This demonstrates the reproducibility of our sputtering deposition.

We employed RBS to measure the chemical compositions of Samples A, B, C, and D, with their Eu/Fe ratios being 0.498, 0.532, 0.578, and 0.586, respectively, as listed in Table I. Note that the stoichiometric Eu/Fe ratio of EuIG ($Eu_3Fe_5O_{12}$) is 0.6. Figure 3(a) shows the $a_{\perp,f,\text{strained}}$ values versus the Eu/Fe ratios, indicating a linear increase of $a_{\perp,f,\text{strained}}$ from 12.561 to 12.600 Å, with the Eu/Fe ratio ranging from 0.498 to 0.586. The fitting details of RBS data are displayed in Supplemental Material Fig. S2 [21]. The Eu/Fe ratio of Sample E is 0.646, as extrapolated from Fig. 3(a). We attribute the monotonic rise of lattice constants with increasing Eu content to the larger ionic radius of Eu^{3+} (0.107 nm) than that of Fe^{3+}(0.064 nm) [27]. For the studied

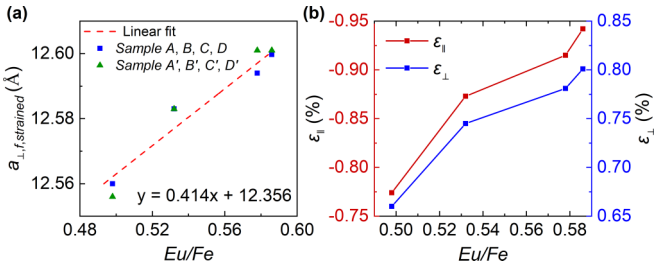

FIG. 3. (a) $a_{\perp,f,\text{strained}}$ of EuIG films versus Eu/Fe values. The Eu/Fe ratio is at.% of Eu divided by at.% of Fe in the sample. The red dashed line is a linear fit to the four data points. (b) Plots of $\varepsilon_{\parallel}$ and $\varepsilon_{\perp}$ versus the Eu/Fe ratio.

Fe-rich EuIG films, the excessive Fe would occupy the Eu at the dodecahedral site, leading to a decrease in $a_{\perp,f,\text{strained}}$ [28,29].

It was reported that the variation of the Tm/Fe ratio in TmIG thin films affected the magnetic properties [9,17]. In this work, we tuned the Eu/Fe ratio to attain the desirable film strain, and thus to manipulate the magnetic properties. Figure 3(b) shows $\varepsilon_{\parallel}$ and $\varepsilon_{\perp}$, as listed in Table I, versus the Eu/Fe ratio for Samples A, B, C, and D. In our EuIG films, the film strain increases with the Eu/Fe ratio.

B. Magnetic properties

1. PMA measured from M-H loops using VSM

Figure 4(a)–4(d) shows a sequence of OOP M-H hysteresis loops of Samples A, B, C, and D with Eu/Fe ratios of 0.498, 0.532, 0.578, and 0.586, respectively. M_s values for these samples were measured to be ∼72, 95, 121, and 125 emu/cm^3, respectively, as listed in Table I. Figure 4(e) shows an IP M-H loop for Sample D.

The 100% squareness of the M-H loops demonstrates the attainment of PMA in the EuIG films. The measured magnetic coercive fields (H_c) of the single-crystal EuIG films in this work increased with an $a_{\perp,f,\text{strained}}$ (thus the Eu/Fe ratio) from 27 to 158 Oe, but decreased to 83 Oe for Sample D with an $a_{\perp,f,\text{strained}}$ of 12.6 Å. The values of M_s and H_c versus Eu/Fe ratios are plotted in Fig. 4(f).

Note that the M_s value for the bulk EuIG is 93 emu/cm^3. The M_s value for the PLD EuIG (Eu/Fe ratio = 0.72) films are 110 emu/cm^3 [on GGG(111)] and 120 emu/cm^3

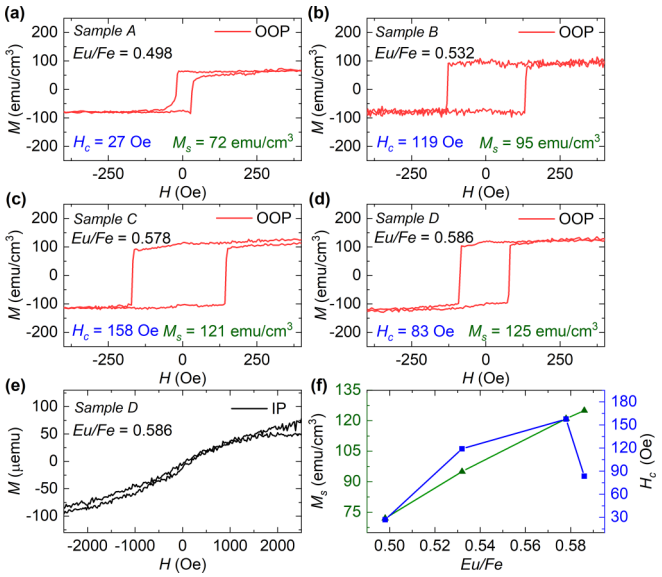

FIG. 4. OOP M-H loops for Samples A, B, C, and D with Eu/Fe ratios of (a) 0.498, (b) 0.532, (c) 0.578, and (d) 0.586. The linear background from the GGG substrate was subtracted. M_s was measured and marked at the bottom of each panel. (e) An IP M-H loop for Sample D with an Eu/Fe ratio of 0.586. Note that its linear background was not subtracted because it has not reached magnetic saturation in this field range, and the y-axis refers to the total magnetization. (f) M_s and H_c versus Eu/Fe ratios.

[on GGG(001)] [20], and those for other PLD EuIG films ranged from 70 to 74 emu/cm^3 [on GGG(001)], depending on the film thickness [10]. For EuIG, the Eu dodecahedral site couples ferromagnetically with the Fe octahedral site, which is coupled antiferromagnetically with the Fe tetrahedral site. Rosenberg *et al.* [20] observed the coexistence of Eu^{2+} and Eu^{3+} in EuIG film. We observed the presence of Eu^{2+} and Eu^{3+} in our samples by x-ray photoemission. The magnetic moment of Eu^{2+} (M_{Eu2+}) is larger than that of Fe^{3+}(M_{Fe3+}), which is larger than that of Eu^{3+} (M_{Eu3+})—namely, the magnitude of the magnetic moment relation being $M_{Eu2+} > M_{Fe3+} > M_{Eu3+}$ [30–32]. In the Fe-rich films, the measured smaller saturation magnetizations indicate that the excess Fe^{3+} may occupy the Eu^{2+} dodecahedral site.

In comparison, the H_c values for the PLD EuIG (Eu/Fe ratio = 0.72) films on GGG(001) were ~400 Oe (56 nm thick) and ~100 Oe (26 nm), while those for the films on GGG(111) were 20 Oe (56 nm) and <5 Oe (26 nm) [20]. The H_c for the 38-nm-thick PLD EuIG film on GGG(001) was ~750 Oe [10].

2. *PMA of EuIG films via XAS/XMCD*

To probe the PMA of our EuIG films further, we carried out XMCD measurements, with a schematic shown in Fig. 5(a), to examine whether the magnetic moment has an IP component in our films. A sample (B*) 12.52 nm in thickness was grown under the same condition as Sample B, followed by the

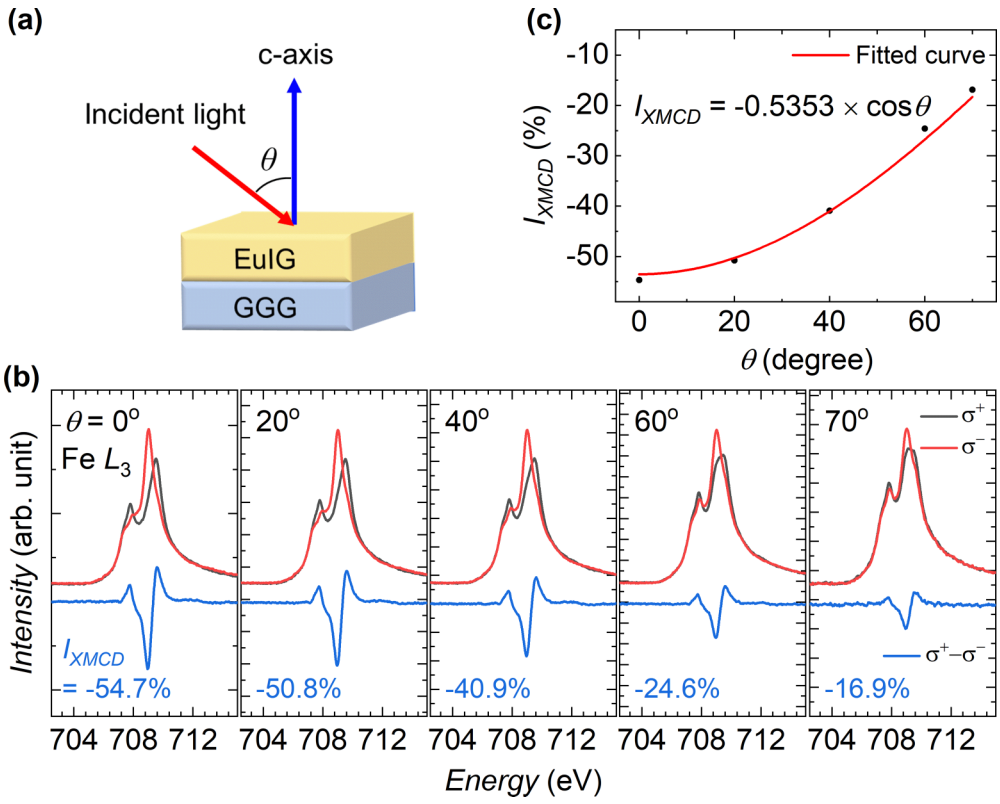

FIG. 5. Angle-dependent XAS and XMCD spectra of the Fe L_3 edge on the EuIG film (Sample B*) measured at 300 K. (a) The incident angle's geometry configuration to the surface normal. (b) The angle-dependent XMCD spectra taken at the Fe L_3 edge, with σ^+ and σ^- denoting the two XAS spectra taken at oppositely polarized light. The relative I_{XMCD} of Fe_{tet} is calculated from the height of XMCD divided by the height of XAS of Fe L_3. (c) The summary of I_{XMCD} results in (b); the red line is a cosine fitting to the data.

deposition of a 2-nm-thick Ti layer by e-beam evaporation. Figure 5(b) shows the angle-dependent XAS and XMCD of the Fe L_3 edge. The negative peak at a photon energy of 709 eV is from the Fe ions located at the tetrahedral sites (Fe_{tet}). The two positive peaks next to the negative peak are from the Fe ions located at octahedral sites (Fe_{oct}). The results indicate that Fe_{oct} is antiferromagnetically coupled to Fe_{tet} [33,34]. The relative XMCD intensity (I_{XMCD}) is largest at the normal incidence (zero incident angle) configuration—namely, the moment parallel to the incident light. The I_{XMCD} decreases with the increasing incident angle. Figure 5(c) plots the I_{XMCD} as a function of incident angle, and the data can be fitted very well by a simple cosine function. This XMCD result demonstrates the PMA of the EuIG film, which has no IP component.

3. Strength of PMA via SMR

To evaluate quantitatively the strength of the PMA of the EuIG films, we extracted $H_\perp$ utilizing electrical transport measurements on sputtered Pt (3-nm-thick)/EuIG films. The samples were patterned into a Hall bar geometry with 650 μm in length and 50 μm in width using standard photolithography.

We performed the SMR measurements of a series of Pt/EuIG bilayers of various Eu/Fe ratios with the IP magnetic field applied transversely to the current. The longitudinal MR ratio $\Delta R_{xx}/R_{xx}(0)$ versus IP magnetic field (H_y) along the y-axis is plotted in Fig. 6(a)–6(d), where $\Delta R_{xx} = R_{xx}(H) - R_{xx}(0)$. According to SMR theory, when the magnetization is aligned in the y direction by the applied field, the resistance reaches the minimum because of less spin absorption at the interface. Thus, by applying the relationship

$$H_{\text{in-sat}} = H_\perp - 4\pi M_s, \tag{4}$$

where $H_{\text{in-sat}}$ stands for the IP saturation field, the PMA strength ($H_\perp$) values of Sample A″ (9.7 nm in thickness), B″ (10.5 nm), C″ (12.5 nm), and D″ (13 nm) were measured to be 4.21, 10.95, 15.97, and 18.87 kOe, respectively, as listed in Table I. Note that Samples A″, B″, C″, and D″ were prepared in the same sputtered conditions as Samples A, B, C, and D, respectively. We therefore expect that the Eu/Fe ratios, the $a_{\perp,f,\text{strained}}$ values, and the film strains are similar between these two sets of samples. The larger $\varepsilon_\parallel$ (or equivalently $\varepsilon_\perp$), as caused by the increase of Eu in the film, has enhanced $H_\perp$, as shown in Fig. 6(e) and 6(f).

In comparison, the $H_\perp$ values attained in the single-crystal TmIG films (24.5 nm in thickness) by Wu *et al.* [9] ranged from 1.43 to 2.44 kOe. The $H_\perp$ values for the PLD EuIG films by Ortiz *et al.* [10] were thickness dependent, ranging from 4.13 kOe (56 nm) to 32.9 kOe (4 nm).

4. Spin mixing conductance and current-induced magnetization switching

The transport and current-induced switching measurements were carried out on the Pt (3 nm)/EuIG (9.7 nm) (Sample A″) sample with the aforementioned Hall bar geometry. According to SMR theory [35], the transverse Hall resistivity (ρ_{trans}) in an HM/MI bilayer can be expressed as

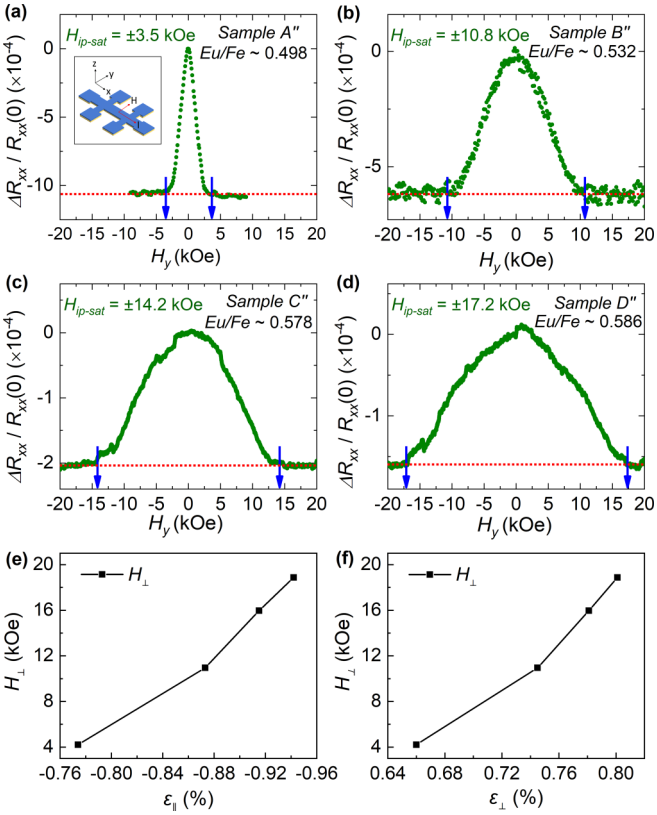

FIG. 6. SMR measurement of Pt/EuIG bilayer structures with the IP field transverse to the current, as indicated in the inset of (a). (a–d) The results of $\Delta R_{xx}/R_{xx}$ as a function of H_y for the EuIG films of Sample A″, B″, C″, and D″, with Eu/Fe ratios of ~0.498, ~0.532, ~0.578, and ~0.586, respectively. The blue arrows mark the H_{ip-sat} of each sample with the values shown at the top of each panel. (e) Plot of $H_\perp$ versus $\varepsilon_\parallel$. (f) Plot of $H_\perp$ versus $\varepsilon_\perp$.

follows:

$$\rho_{\text{trans}} = \Delta\rho_1 m_x m_y + \Delta\rho_2 m_z, \tag{5}$$

where m_i denotes the i component of the unit magnetization of EuIG. From $\Delta\rho_1$ and $\Delta\rho_2$, we arrive at the following relations:

$$\frac{\Delta\rho_1}{\rho} = {\theta_{SH}}^2 \frac{\lambda}{d_N} \frac{2\lambda G_r \tanh^2 \frac{d_N}{2\lambda}}{\sigma + 2\lambda G_r \coth \frac{d_N}{\lambda}}, \tag{6}$$

and

$$\frac{\Delta\rho_2}{\rho} \approx {\theta_{SH}}^2 \frac{\lambda}{d_N} \frac{2\lambda\sigma G_i \tanh^2 \frac{d_N}{2\lambda}}{\left(\sigma + 2\lambda G_r \coth \frac{d_N}{\lambda}\right)^2}, \tag{7}$$

where ρ, σ, d_N, λ, θ_{SH}, G_r, and G_i represent Pt longitudinal resistivity, conductivity, thickness of the metal layer, spin diffusion length, spin Hall angle, and the real and imaginary parts of spin mixing conductance, respectively. First, we measured the SMR-induced anomalous Hall signal with the OOP magnetic field at room temperature. Good squareness of the AHE loop with the AHE loop coercivity (H_c^{AHE}) of 65 Oe is clearly shown in Fig. 7(b). From the amplitude of the AHE signal, we then obtained $\Delta\rho_2 = 9.63 \times 10^{-4}$ $\mu\Omega$-cm. Next, we measured the IP angular-dependent transverse

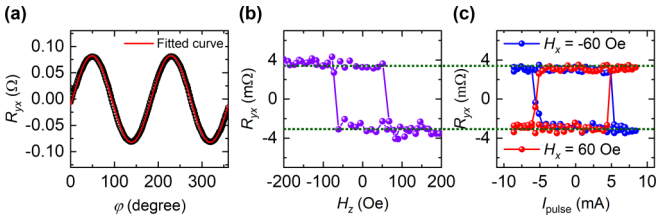

FIG. 7. (a) IP angle-dependent SMR for the Pt/EuIG (Sample A″) sample with a 10-kOe applied field. (b), (c) AHE measurement and current-induced switching measurement, respectively.

resistance displayed in Fig. 7(a), and $\Delta\rho_1 = 4.94 \times 10^{-2}\,\mu\Omega$-cm was extracted from the fitting result; $\rho = 67.5\,\mu\Omega$-cm was measured in the same Hall bar. We assumed $\lambda = 1.4$ nm and $\theta_{SH} = 0.08$ [36,37]. The values of G_r and G_i are determined to be $3.48 \times 10^{14}\,\Omega^{-1}\,m^{-2}$ and $1.13 \times 10^{13}\,\Omega^{-1}\,m^{-2}$, respectively. Note that the previous work by Rosenberg *et al.* [20] reported the lower bound of G_i to be $5.4 \times 10^{12}\,\Omega^{-1}\,m^{-2}$ of Pt/EuIG/GGG(001) according to their AHE measurement, and the G_r from the reference of Pt/TmIG. Here, by measuring both SMR-induced AHE and IP angular-dependent SMR, we directly obtained the precise G_r and G_i values of the Pt/EuIG interface.

Current-induced magnetization switching was demonstrated on the same device with the transport measurement. Figure 7(c) shows the switching results with a H_x of ±60 Oe. This external H_x breaks the switching symmetry and overcomes the interfacial Dzyaloshinskii–Moriya interaction effective field. Compared to the AHE loop, the magnetization of EuIG is fully switched by the pulsed current-induced spin-orbit torque from Pt. The critical current density (J_c) is $3.5 \times 10^6\,A/cm^2$, which is lower than the values obtained in Pt/TmIG ($J_c = 1.8 \times 10^7$, $6.0 \times 10^6\,A/cm^2$) by Avci *et al.* [37], and is comparable to the value of $J_c = 2.5 \times 10^6\,A/cm^2$ by Wu *et al.* [9]. The lower critical current density could be attributed to the higher G_r, which gives rise to the higher efficiency of spin transmission at the interface. This has been achieved by the relatively small H_c and M_s that can be precisely adjusted by manipulating the Eu/Fe ratio.

IV. CONCLUSION

Single-crystal EuIG thin films with excellent crystallinity and a smooth surface were epitaxially grown on GGG(001) using off-axis sputtering. Fully strained EuIG epi films on GGG have shown PMA, which was established by both the squarish OOP M-H loop and the angle-dependent XMCD measurement. Clear SMR-induced AHE loops with good squareness were measured through the spin transport measurement, enabling the determination of the $H_\perp$ values (PMA strength) of the insulating EuIG films. The PMA strength was well correlated with the measured/calculated film strain, which was tuned with the Eu/Fe ratio in the film. For EuIG films possessing suitably low H_c, we have fabricated a Pt/EuIG structure to attain a low switching current density for current-induced PMA magnetization switching, suggesting the potential for constructing low-dissipation spintronic devices. Also, the sputtering technique is advantageous as it can be scaled up for industrial applications.

ACKNOWLEDGMENTS

We thank Dr. C. T. Chen and Prof. C. Y. Kuo for their valuable contributions to the XMCD experiment in the 45A beamline at NSRRC. We acknowledge technical support from NGPL/IOP/Academia Sinica, NSRRC, TSRI, and the NTU Consortium of Electron Microscopy Key Technology, Taiwan. This work was supported by the Ministry of Science and Technology, Taiwan (Grants No. 110-2112-M-002-036- and No. 110-2622-8-002-014-); the Center for Quantum Technology, NTHU (Project No. 111B0018I4); and the Center for Complex Phase Materials, NTHU (Project No. 111Q214CE1). We also acknowledge support from the Max Planck-POSTECH-Hsinchu Center for Complex Phase Materials.

[1] Y. Kajiwara *et al.*, Nature (London) **464**, 262 (2010).
[2] Y. Sun, H. Chang, M. Kabatek, Y.-Y. Song, Z. Wang, M. Jantz, W. Schneider, M. Wu, E. Montoya, B. Kardasz, B. Heinrich, S. G. E. teVelthuis, H. Schultheiss, and A. Hoffmann, Phys. Rev. Lett. **111**, 106601 (2013).
[3] H. Nakayama, M. Althammer, Y.-T. Chen, K. Uchida, Y. Kajiwara, D. Kikuchi, T. Ohtani, S. Geprägs, M. Opel, S. Takahashi, R. Gross, G. E. W. Bauer, S. T. B. Goennenwein, and E. Saitoh, Phys. Rev. Lett. **110**, 206601 (2013).
[4] M. C. Onbasli, A. Kehlberger, D. H. Kim, G. Jakob, M. Kläui, A. V. Chumak, B. Hillebrands, and C. A. Ross, APL Mater. **2**, 106102 (2014).
[5] S. M. Zanjani and M. C. Onbaşlı, J. Magn. Magn. Mater. **499**, 166108 (2020).
[6] M. Kubota, A. Tsukazaki, F. Kagawa, K. Shibuya, Y. Tokunaga, M. Kawasaki, and Y. Tokura, Appl. Phys. Express **5**, 103002 (2012).
[7] E. Popova, N. Keller, F. Gendron, L. Thomas, M.-C. Brianso, M. Guyot, M. Tessier, and S. S. P. Parkin, J. Vac. Sci. Technol. A **19**, 2567 (2001).
[8] J. Fu *et al.*, Appl. Phys. Lett. **110**, 202403 (2017).
[9] C. N. Wu *et al.*, Sci. Rep. **8**, 11087 (2018).
[10] V. H. Ortiz, M. Aldosary, J. Li, Y. Xu, M. I. Lohmann, P. Sellappan, Y. Kodera, J. E. Garay, and J. Shi, APL Mater. **6**, 121113 (2018).
[11] C. Tang, P. Sellappan, Y. Liu, Y. Xu, J. E. Garay, and J. Shi, Phys. Rev. B **94**, 140403(R) (2016).
[12] C. O. Avci, A. Quindeau, C.-F. Pai, M. Mann, L. Caretta, A. S. Tang, M. C. Onbasli, C. A. Ross, and G. S. D. Beach, Nat. Mater. **16**, 309 (2017).
[13] A. Quindeau *et al.*, Adv. Electron. Mater. **3**, 1600376 (2017).
[14] Y. K. Liu, H. F. Wong, K. K. Lam, K. H. Chan, C. L. Mak, and C. W. Leung, J. Magn. Magn. Mater. **468**, 235 (2018).
[15] Q. Shao, A. Grutter, Y. Liu, G. Yu, C.-Y. Yang, D. A. Gilbert, E. Arenholz, P. Shafer, X. Che, C. Tang, M. Aldosoary, A. Navabi, Q. L. He, B. J. Kirby, J. Shi, K. L. Wang, Phys. Rev. B **99**, 104401 (2019).
[16] S. Xia, S. Zhang, Z. Luan, L. Zhou, J. Liang, G. Liu, B. Yang, H. Yang, R. Liu, and D. Wu, Appl. Phys. Lett. **116**, 052404 (2020).

[17] C. N. Wu, C. C. Tseng, K. Y. Lin, C. K. Cheng, S. L. Yeh, Y. T. Fanchiang, M. Hong, and J. Kwo, AIP Adv. **8**, 055904 (2018).
[18] C. Tang *et al.*, Sci. Adv. **3**, e1700307 (2017).
[19] S. R. Yang, Y. T. Fanchiang, C. C. Chen, C. C. Tseng, Y. C. Liu, M. X. Guo, M. Hong, S. F. Lee, and J. Kwo, Phys. Rev. B **100**, 045138 (2019).
[20] E. R. Rosenberg, L. Beran, C. O. Avci, C. Zeledon, B. Song, C. Gonzalez-Fuentes, J. Mendil, P. Gambardella, M. Veis, C. Garcia, G. S. D. Beach, and C. A. Ross, Phys. Rev. Mater. **2**, 094405 (2018).
[21] See Supplemental Material at http://link.aps.org/supplemental/10.1103/PhysRevMaterials.6.054412 for figures showing the off-axis rf magnetron sputtering setup and RBS composition analysis results.
[22] S. Emori, E. Martinez, K.-J. Lee, H.-W. Lee, U. Bauer, S.-M. Ahn, P. Agrawal, D. C. Bono, and G. S. D. Beach, Phys. Rev. B **90**, 184427 (2014).
[23] O. J. Lee, L. Q. Liu, C. F. Pai, Y. Li, H. W. Tseng, P. G. Gowtham, J. P. Park, D. C. Ralph, and R. A. Buhrman, Phys. Rev. B **89**, 024418 (2014).
[24] W.-J. Zou *et al.*, ACS Nano **16**, 2369 (2022).
[25] J. Sasvári and P.-E. Werner, Acta Chem. Scand. A **37**, 203 (1983).
[26] E. L. Dukhovskaya, Y. G. Saksonov, and A. G. Titova, Izv. Akad. Nauk SSSR, Neorg. Mater. **9**, 809 (1973).
[27] S. Sakaida, Y. Shimokawa, T. Asaka, S. Honda, and Y. Iwamoto, Mater. Res. Bull. **67**, 146 (2015).
[28] R. H. Langley and G. D. Sturgeon, J. Solid State Chem. **30**, 79 (1979).
[29] S. Geller, J. P. Remeika, R. C. Sherwood, H. J. Williams, and G. P. Espinosa, Phys. Rev. **137**, A1034 (1965).
[30] K. S. Kumar and C. Venkateswaran, IOP Conf. Ser. Mater. Sci. Eng. **73**, 012031 (2015).
[31] S.-W. Kim, H. Kim, J.-K. Kim, W.-S. Noh, J. Kim, K.-M. Kim, K.-S. Kim, J. S. Kim, J.-H. Park, and M.-H. Jung, APL Mater. **8**, 111108 (2020).
[32] Y. Takikawa, S. Ebisu, and S. Nagata, J. Phys. Chem. Solids **71**, 1592 (2010).
[33] P. Rudolf, F. Sette, L. H. Tjeng, G. Meigs, and C. T. Chen, J. Magn. Magn. Mater. **109**, 109 (1992).
[34] Y. Y. Chin, H.-J. Lin, Y.-F. Liao, W. C. Wang, P. Wang, D. Wu, A. Singh, H.-Y. Huang, Y.-Y. Chu, D. J. Huang, K. D. Tsuei, C. T. Chen, A. Tanaka, and A. Chainani, Phys. Rev. B **99**, 184407 (2019).
[35] Y.-T. Chen, S. Takahashi, H. Nakayama, M. Althammer, S. T. B. Goennenwein, E. Saitoh, and G. E. W. Bauer, Phys. Rev. B **87**, 144411 (2013).
[36] L. Liu, T. Moriyama, D. C. Ralph, and R. A. Buhrman, Phys. Rev. Lett. **106**, 036601 (2011).
[37] C. O. Avci, E. Rosenberg, M. Baumgartner, L. Beran, A. Quindeau, P. Gambardella, C. A. Ross, and G. S. D. Beach, Appl. Phys. Lett. **111**, 072406 (2017).